JOURNAL OF SOLID STATE CHEMISTRY 71, 244–262 (1987)

Structural and Electronic Properties of Transition Metal Thiophosphates

M. EVAIN AND R. BREC

Laboratoire de Chimie des Solides, U.A. 279, Université de Nantes, 44072 Nantes Cédex, France

AND M.-H. WHANGBO

Department of Chemistry, North Carolina State University, Raleigh, North Carolina 27695-8204

Received December 29, 1986

From the viewpoint of metal coordination we examine the structural characteristics of several new members of transition metal thiophosphates (i.e., M–P–S phases with M = V, Nb, Ta), in which various ligands such as S^{2-}, S_2^{2-}, and phosphorus–sulfur polyanions $P_nS_m^{x-}$ ($1 \le n \le 4$; $3 \le m \le 13$; $2 \le x \le 6$) provide either an octahedral or a bicapped prismatic coordination of the metal. Tight-binding band electronic structure calculations show that the low-lying acceptor orbitals responsible for lithium intercalation of thiophosphates are their d-block bands. This prediction is confirmed by our electrochemical lithium intercalation study which reveals that the reduction sites of thiophosphates are their metal cations. Molecular orbital calculations are carried out on vanadium compounds with extremely short interligand S···S contacts. The occurrence of such short contact distances is not caused by covalent bonding in the S···S contacts but by the small size of vanadium cations which forces its surrounding sulfur ligands to squeeze one another.

1. Introduction

With phorphorus and transition metal, chalcogens are found to form mostly low-dimensional compounds. The well-known example of these thiophosphates is the family of two-dimensional compounds MPS_3 (e.g., M = Mn, Fe, Co, Ni, Zn) (*1–3*), first synthesized and characterized more than two decades ago (*4, 5*). Several new members of transition metal thiophosphates have recently been prepared, which include a one-dimensional (1D) compound PV_2S_{10} (*6*), two-dimensional (2D) compounds $P_{0.2}VS_2$ (*7, 8*), $V_2P_4S_{13}$ (*9*), PNb_2S_{10} (*10*), $P_2Nb_4S_{21}$ (*11*), and P_2NbS_8 (*12*), and three-dimensional (3D) compounds P_2NbS_8 (*13*), $TaPS_6$ (*14*), and $Ta_4P_4S_{29}$ (*15*).

Transition metal thiophosphates are of potential importance as low-dimensional oxidizing materials for secondary lithium batteries (*16, 17*). In understanding the lithium intercalation behavior of these compounds, it is necessary to know their electronic structures. Except for the MPS_3 phases (*18, 19*), however, no electronic structure calculations have been performed on any transition metal thiophosphates. Thus in the present work, we examine the structural characteristics and the electronic

0022-4596/87 $3.00

properties of these compounds. In Section 2, the crystal structures of various transition metal thiophosphates are described in terms of metal coordination with S^{2-}, S_2^{2-}, and phosphorus–sulfur polyanion ligands. Discussed in Section 3 are the electronic structures of those thiophosphates, which were obtained by performing extended Hückel molecular orbital (*20*) and tight-binding band orbital calculations (*21, 22*). The atomic parameters employed in our study are summarized in Table I. Based upon the findings in Sections 2 and 3, we briefly discuss the lithium intercalation characteristics of PV_2S_{10} and $V_2P_4S_{13}$ in Section 4.

2. Structural Characteristics

The structures of transition metal thiophosphates are conveniently described in terms of their metal coordination. The ligands that have been found to form the thiophosphates are S^{2-}, S_2^{2-}, and various phosphorus–sulfur polyanions PS_3^{3-} (**1**), PS_4^{3-} (**2**), $P_2S_6^{2-}$ (**3**), $P_2S_6^{4-}$ (**4**), $P_2S_8^{4-}$ (**5**), $P_2S_9^{4-}$ (**6**), $P_4S_{12}^{4-}$ (**7**), and $P_4S_{13}^{6-}$ (**8**) (see Schemes 1–8 in Chart I). To date, those ligands have been found to provide either an octahedral or a bicapped prismatic coordination of metal. The structural patterns of transition metal thiophosphates are briefly summarized in the following.

2.1. *Octahedral Coordination*

MPS_3 (M = Mn, Fe, Co, Ni, Zn) phases contain layers of composition $(M^{2+})_2(P_2S_6^{4-})$ (*1–3*). Shown in **9a** is a projection view of the $P_2S_6^{4-}$ anion **4** along the P–P bond axis. With this representation of **4** (i.e., **9a**), an MPS_3 layer is given by **9b**, where three $P_2S_6^{4-}$ ions surround each M^{2+} ion, thereby

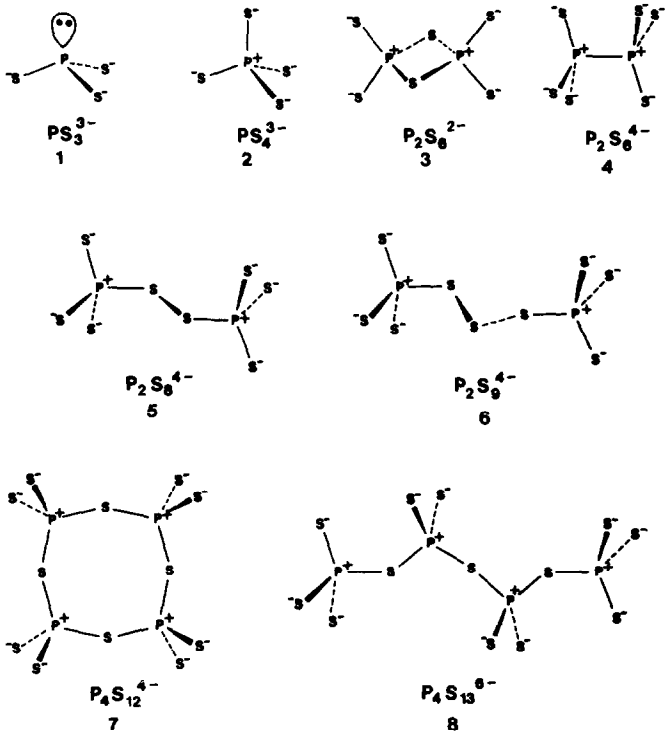

CHART I

TABLE I

EXPONENTS ζ_μ AND VALENCE-SHELL IONIZATION POTENTIALS $H_{\mu\mu}$ FOR SLATER-TYPE ORBITALS χ_μ

χ_μ	ζ_μ	ζ'_μ	$H_{\mu\mu}$ (eV)
V 4*s*	1.3		−8.8
V 4*p*	0.9		−5.8
V 3*d*	4.75 (0.4755)	1.7 (0.7052)	−11.10
Nb 5*s*	1.89		−10.10
Nb 5*p*	1.85		−6.86
Nb 4*d*	4.08 (0.6401)	1.64 (0.5516)	−12.10
Ta 6*s*	2.28		−10.10
Ta 6*p*	2.24		−6.86
Ta 5*d*	4.76 (0.6597)	1.94 (0.5589)	−12.10
S 3*s*	2.12		−20.10
S 3*p*	1.83		−13.30
P 3*s*	1.88		−20.20
P 3*p*	1.63		−12.50

Note. The *d*-orbitals of MO are given as a linear combination of two Slater-type orbitals (*35*) and each is followed by weighting factors in parentheses. A modified Wolfsberg–Helmholz formula was used to calculate $H_{\mu\nu}$ (*36*).

providing an octahedral coordination for M^{2+}. A slight modification of the MPS_3 structure is found for $V_{0.78}PS_3$ (*23*) which results when some metal sites of each MPS_3 layer are vacant.

$P_{0.2}VS_2$ (*8*) has a structure closely related to the layer compound TiS_2. In each layer of $P_{0.2}VS_2$, each V is octahedrally coordinated by S^{2-} and/or PS_3^{3-} (**1**). Most V atoms are surrounded by six S^{2-} anions as shown in **10a**, but some V atoms are surrounded by three S^{2-} and one PS_3^{3-} anions as shown in **10b**.

$V_2P_4S_{13}$ (*9*) contains layers made up of the polyanion $P_4S_{13}^{6-}$ (**8**). Each $-P^+(S^-)_3$

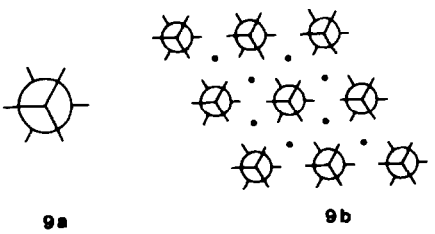

9a **9b**

SCHEME 9

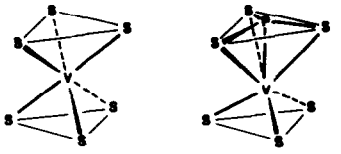

10a **10b**

SCHEME 10

group of **8** provides three coordination sites, and each $-P^+(S^-)_2-$ group of **8** two coordination sites. As schematically shown in **11a**, every two V^{3+} ions of $V_2P_4S_{13}$ are located in a cage of 10 sulfur atoms (i.e., two edge-sharing octahedra of 10 sulfur atoms), which are made up of four polyanions **8**. To form this sulfur cage, two polyanions utilize their $-P^+(S^-)_3$ groups, and the other two their $-P^+(S^-)_2-$ groups. A single layer of $V_2P_4S_{13}$ is shown in **11b**, where each polyanion **8** participates in making four dif-

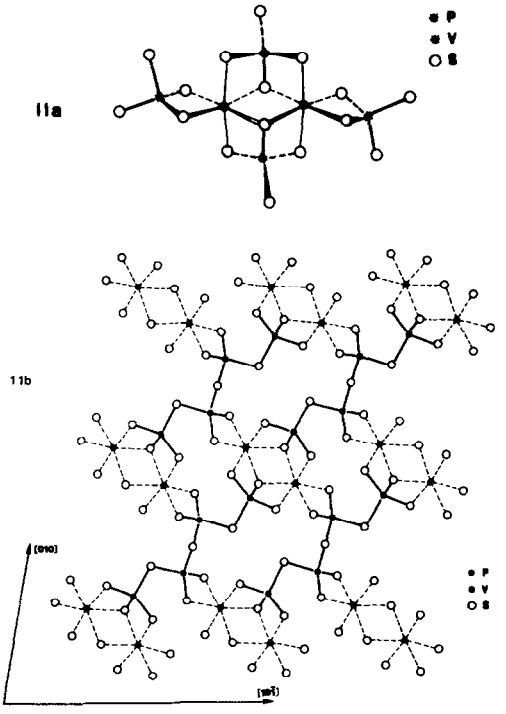

SCHEME 11

ferent sulfur cages. In each sulfur cage, the distance between the two V^{3+} ions is long (3.72 Å), so that there is no direct metal–metal bonding between the two V^{3+} ions.

2.2. *Bicapped Prismatic Coordination*

A bicapped prismatic coordination of metal (**12a**) is typically found for layered chalcogenides MX_3 (e.g., M = Ti, Zr, Hf, V, Nb, Ta; X = S, Se) (*24, 25*). As shown in **12b**, MX_6 prisms share their triangular faces to form an MX_3 prismatic chain. A layer structure of composition MX_3 such as **12c** is obtained when two rectangular faces of each MX_6 prism of a prismatic chain are capped by the chalcogen atoms of two adjacent prismatic chains. In the layered sulfides MS_3, each metal is coordinated by two kinds of anions, S^{2-} and S_2^{2-}. In transition metal thiophosphates, however, bicapped prismatic coordination is provided by S_2^{2-} and the polyanions **2–8**. For those polyanions, a phosphorus atom carries a formal charge of +1, and a sulfur atom that of 0 or −1. It is those sulfur atoms with formal charge of −1 that participate in metal coordination. Due largely to the presence of many different phosphorus–sulfur polyanions, a number of structural varieties exist in transition metal thiophosphates.

2.2.1. Monoprism with three S_2^{2-} anions and one polyanion. Shown in **13a** is a bicapped monoprism that is constructed from three S_2^{2-} anions and a $-P^+(S^-)_3$ group of one polyanion **5** or **6**. Two S_2^{2-} anions occupy four corners of a monoprism, while the third S_2^{2-} anion and the $-P^+(S^-)_3$ group occupy the remaining two corners of the prism as well as cap the two faces of the prism. The latter S_2^{2-} anion and the $-P^+(S^-)_3$ group also form another monoprism, thereby leading to a biprism **13b**. Such biprism units join together upon sharing their rectangular faces to form a "biprism chain," whose projection view along the prism axis is shown in **13c**.

The anions **5** and **6** each have two $-P^+(S^-)_3$ groups, both of which lead to bicapped prismatic coordination. Thus, the two $-P^+(S^-)_3$ ends of **5** or **6** become parts of two different biprism chains, so that biprism chains are linked by sulfur bridges –S–S– or –S–S–S–. The thiophosphates 1D-PV_2S_{10} (*6*), 2D-PNb_2S_{10} (*10*), and 2D-$P_2Nb_4S_{21}$ (*11*) differ in how their biprism chains are joined together by sulfur bridges.

Shown in **14a** is a schematic view of two biprism chains linked by –S–S– bridges. Here each rod represents a biprism chain, and each line connecting the two rods represents a –S–S– bridge. This linking (**14a**) is found for 1D-PV_2S_{10}. A projection view of **14a** along the chain is given by **14b**. Then, the structure of 1D-PV_2S_{10} is represented by **14c**. An alternative way of linking biprism chains by –S–S– bridges is shown in **15a**, where biprism chains are joined so as to form a 2D net structure. This structure is found for 2D-PNb_2S_{10}. Given a projection view of **15a** along the chain axis as **15b**, the structure of 2D-PNb_2S_{10} is represented by **15c**.

The linking pattern of the anion **6**, found for 2D-$P_2Nb_4S_{21}$, is somewhat more complicated than that of the anion **5** described

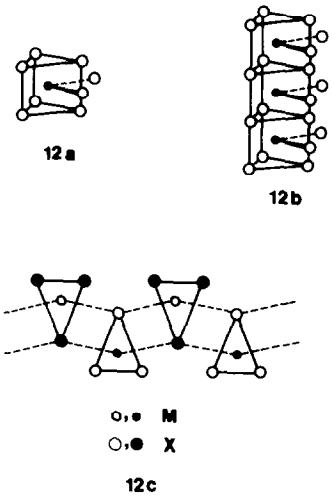

SCHEME 12

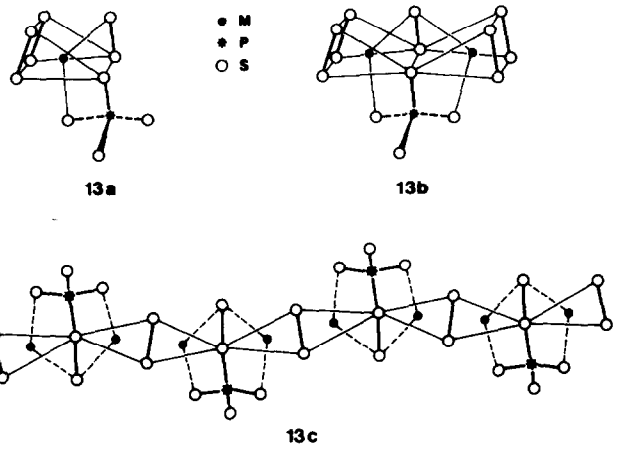

SCHEME 13

above for 1D-PV_2S_{10} and 2D-PNb_2S_{10}. This is caused by the fact that the –S–S–S– bridge of **6** is longer than the –S–S– bridge of **5**. Shown in **16** are two parallel columns of biprism chains without any –S–S–S– bridge between them. These biprism chains may be crosslinked by –S–S–S– bridges as shown in **17a** or **18a**. The projection views of **17a** and **18a** along the chain axis are given by **17b** and **18b**, respectively. When the two crosslinked 2D networks **17** and **18** intertwine, there results a layer structure whose projection view along the chain direction is given by **19a**. Such intertwined 2D networks are packed in 2D-$P_2Nb_4S_{21}$ as shown in **19b**.

2.2.2. Monoprism with two S_2^{2-} anions and two polyanions. Shown in **20a** is a monoprism made up of two S_2^{2-} anions and two polyanions (**2**, **4**, or **7**), where the two S_2^{2-} anions form a rectangular face of the monoprism while the two polyanions oc-

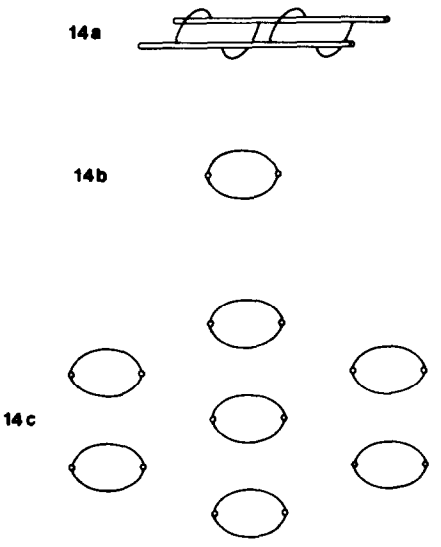

SCHEME 14

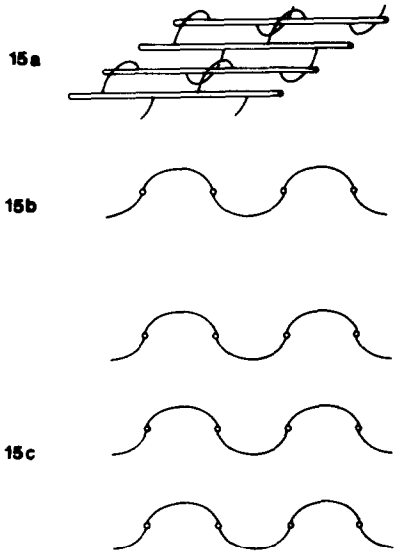

SCHEME 15

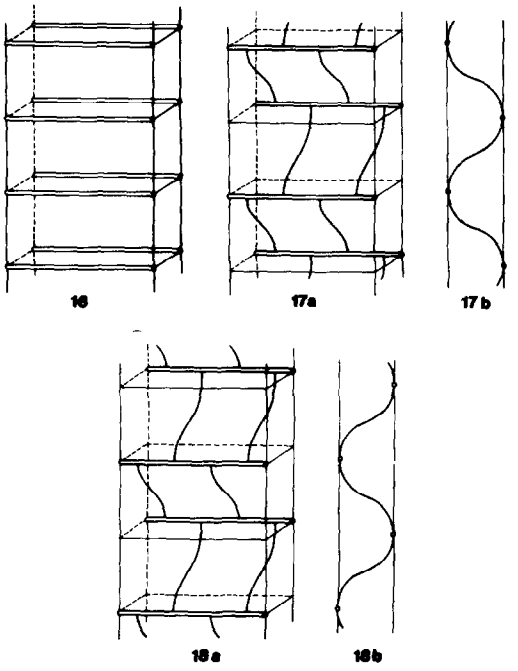

SCHEMES 16–18

cupy the remaining corners of the prism as well as cap the two other rectangular faces of the prism. A projection view of **20a** along the prism axis is shown in **20b**, where it should be noted that the two $-P^{+}(S^{-})_2-$ groups have different heights along the prism axis. When two such monoprisms share their rectangular faces, one obtains two kinds of biprisms, shown in **20c** and **20d**. Ideal prisms **20c** and **20d**, which will be referred to as the "up–up" and "up–down" biprisms, respectively, have symmetry elements of inversion and twofold rotation, respectively.

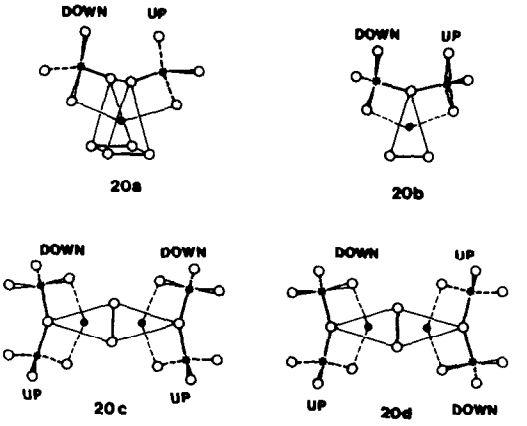

SCHEME 20

Shown in **21** is a schematic diagram for how biprisms made up of the anions **2** link together to form a helix. Each anion **2** connects an upper corner of one biprism to a lower corner of the adjacent biprism, which leads to a helix that has four biprisms per repeat distance. Such a "biprism helix" can be either right- or left-handed. Shown in **22a** are two right-handed biprism helices intertwined to form a channel of empty space, where each biprism unit is represented by a dot. Such biprism "double heli-

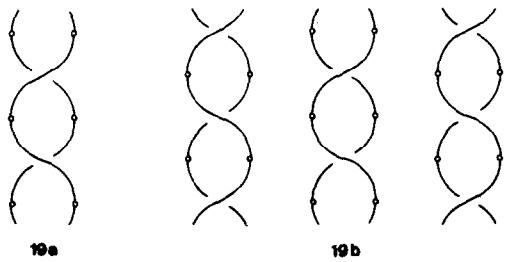

SCHEME 19

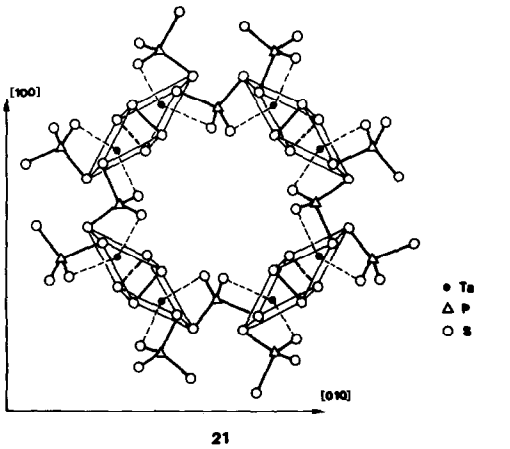

SCHEME 21

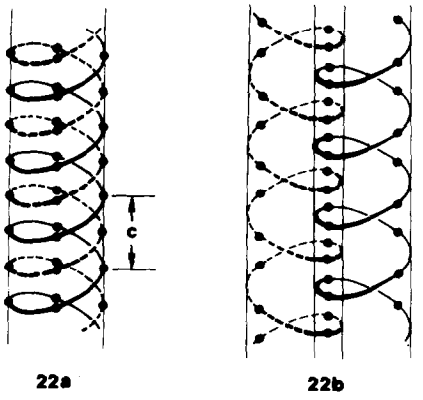

SCHEME 22

ces" are found in $Ta_4P_4S_{29}$ (*15*). The structure of this compound may be best described by considering schematic diagrams **23a–23c**, where a bar in **23a**, or a broken bar in **23b**, at each corner of a square represents a biprism. The fractional numbers at the corners of the squares refer to the heights of the biprisms in units of the repeat distance c of the double helix **22a**, and the curved arrows indicate that the biprisms with a larger channel form a right-handed helix, but those with a smaller channel form a left-handed helix. The structures **23a** and **23b** differ in their heights by $c/2$. It is noted from **23a** and **23b** that each biprism is shared by adjacent helices. A re-

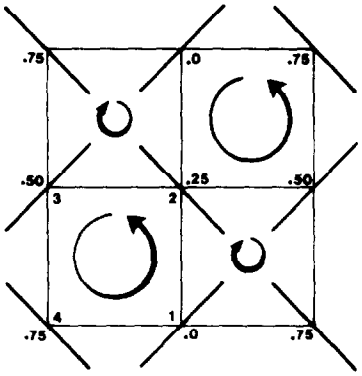

23a

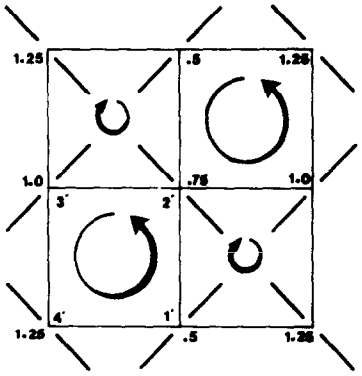

23b

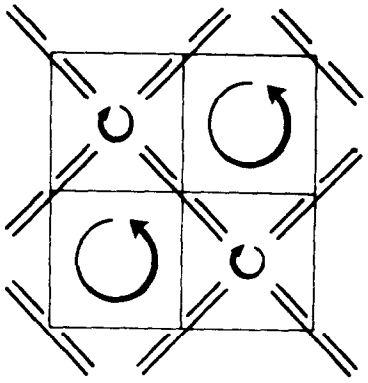

23c

SCHEME 23

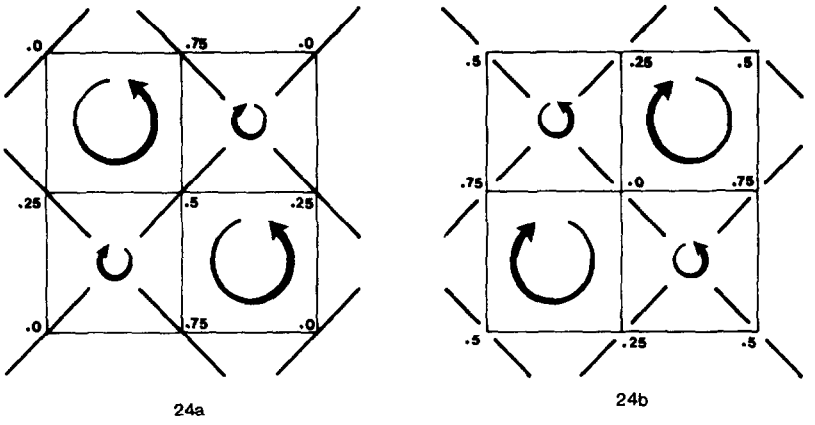

24a 24b

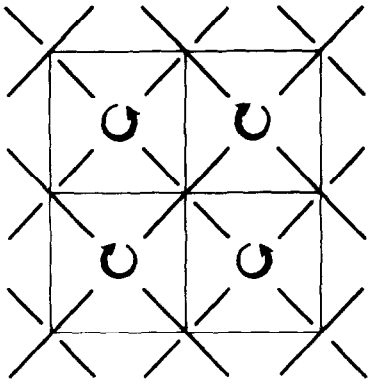

24c

SCHEME 24

peat unit of **23a** or **23b** contains four biprism units, two large "right-handed helix channels" and two small "left-handed helix channels." Since each anion **2** of a biprism is also a part of another prism, **23a** and **23b** have a repeat unit of formula $4[Ta_2(S_2)_2(PS_4)_{4/2}]$. When **23a** and **23b** are intertwined, one obtains a 3D structure **23c**, whose repeat unit now becomes $8[Ta_2(S_2)_2(PS_4)_{4/2}]$. When each of the two large right-handed helix channels of **23c** holds a helix chain $(S_{10})_\infty$, there occurs the compound $Ta_4P_4S_{29}$, i.e., $\{8[Ta_2(S_2)_2(PS_4)_{4/2}] + 2S_{10}\}/4$.

The $(S_{10})_\infty$ chain enclosed in each right-handed helix channel of $Ta_4P_4S_{29}$ is also right-handed. One can consider the possibility of finding left-handed $Ta_4P_4S_{29}$ in which the larger helix channels and the $(S_{10})_\infty$ helix chains are both left-handed.[1] This possibility cannot be discounted. Shown in **22b** is how a right-handed and a

[1] For $Ta_4P_4S_{29}$ both $P4_32_12$ and $P4_12_12$ space groups may account for the observed extinction on X-ray diffraction patterns. Refinements conducted with the $P4_32_12$ and $P4_12_12$ groups correspond to right- and left-hand helices, respectively. Calculations from the $P4_32_12$ group yielded better results (lower R value and improved atomic parameters) and thus the helices were considered as right-handed. However, unambiguous conclusions can only be drawn from full space data recording, leading to absolute configuration. The above result was obtained from a quarter-space recording (*15*).

left-handed helix can intertwine. Such an arrangement is observed when a right-handed structure **24a** and a left-handed structure **24b** are assembled together to form a 3D network **24c**. In this structure, the larger helix channels are destroyed and only the smaller channels remain undestroyed, unlike the case of **23c**. The 3D structure **24c** is found for $TaPS_6$ (*14*), i.e., $8[Ta_2(S_2)_2(PS_4)_{4/2}]/16$.

Another 3D network structure of transition metal thiophosphates is obtained from the cyclic polyanion **7**. An up–down biprism **20d** may be formed from two S_2^{2-} anions and four polyanions **7** in which each polyanion **7** uses only one $-P^+(S^-)_2-$ group. Thus, a single anion **7** holds four biprisms as schematically shown in **25**, where any given anion **7** uses two $-P^+(S^-)_2-$ groups at 1,3-positions for the lower corners of two biprisms and those two at 2,4-positions for the upper corners of two other biprisms.

In 2D-P_2NbS_8 (*12*), four polyanions **3** are employed to form an up–up biprism. Each anion **3** links two such biprisms to construct a layer structure **26a** or **26b**. It is these two layer structures that alternate along the crystallographic *c*-direction in 2D-P_2NbS_8. It is noted that an up–up biprism leads to a 2D network structure, while an up–down biprism leads to a 3D network structure (*13*).

3. Electronic Structure

As discussed in the previous section, transition metal thiophosphates are coordination compounds of transition metal elements V, Nb, and Ta with S_2^{2-} and polyanions **2–8**. In this section, we examine their low-lying acceptor levels. Summarized in Fig. 1 are the molecular orbital (MO) energies for the ligands associated with the thiophosphates, which were calculated by employing the extended Hückel method (*26*). Also shown in Fig. 1 are the valence and the conduction band energies of the $(S_{10})_\infty$ chain. The HOMO of PS_3^{3-} is mainly the phosphorus lone pair, and hence lies somewhat high in energy. The empty levels of all the ligands and the $(S_{10})_\infty$ chain are σ antibonding levels of the P–S, P–P, or

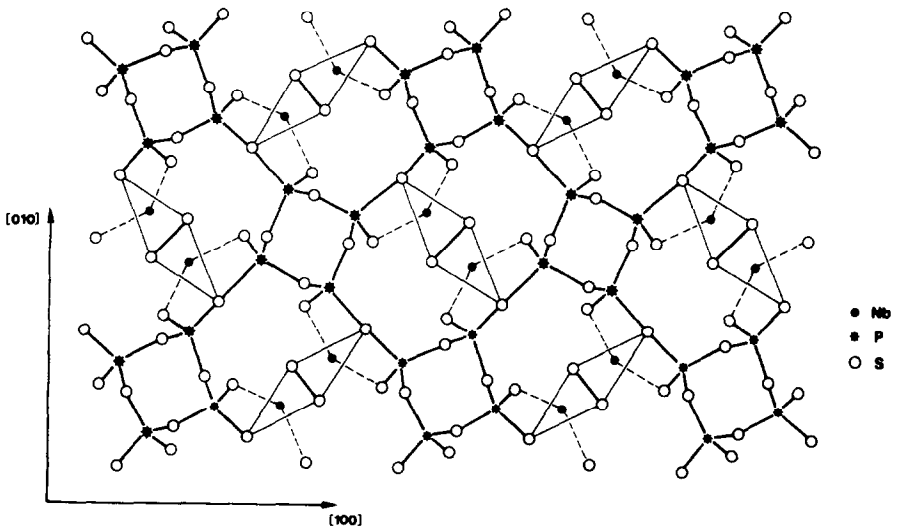

25

SCHEME 25

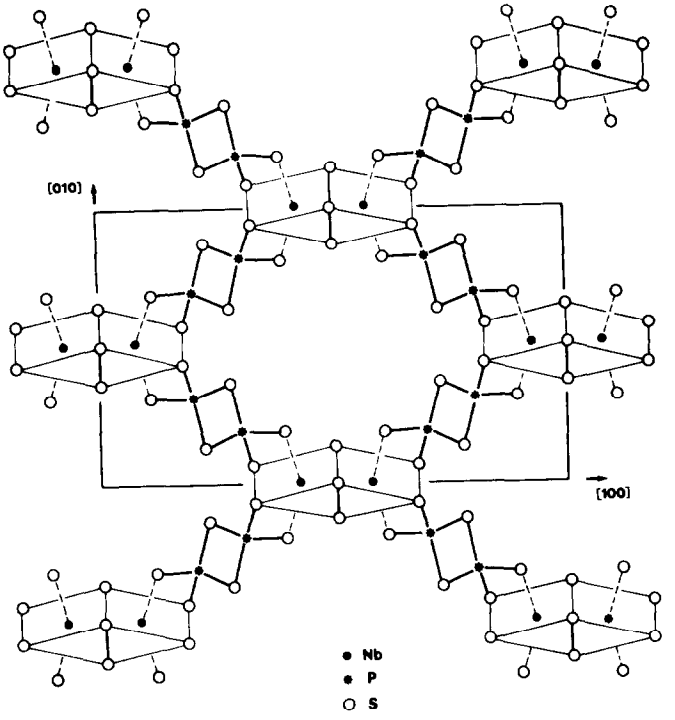

26a

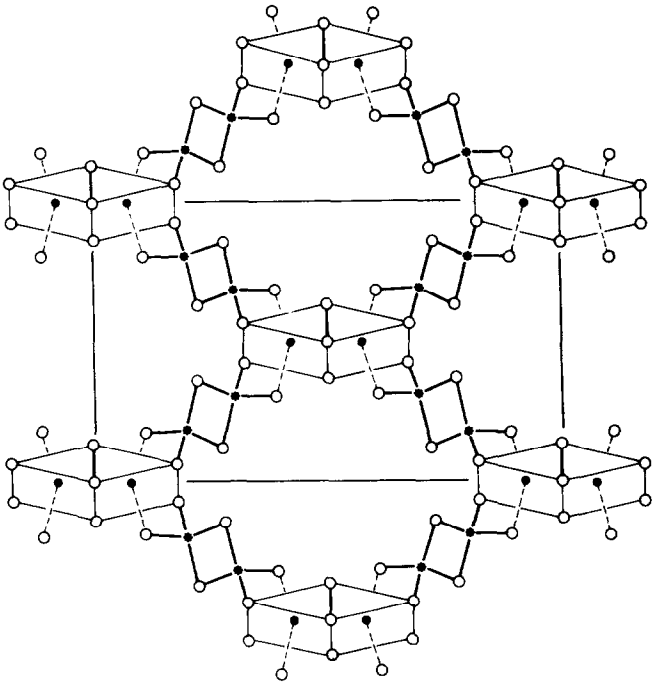

26b

SCHEME 26

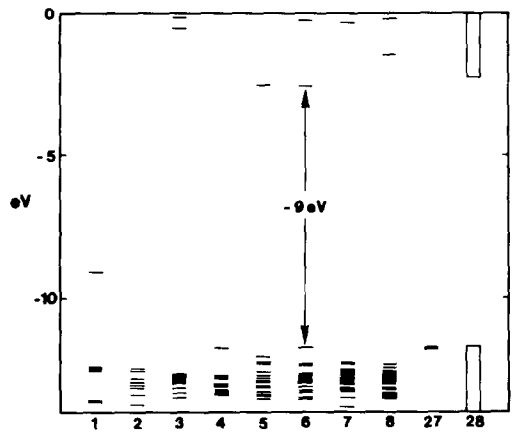

FIG. 1. Calculated MO energies of phosphorus–sulfur polyanions **1–8**, S_2^{2-} (**27**), and $(S_{10})_\infty$ chain (**28**), where the σ^* orbitals of the S–S, P–S, and P–P single bonds occur above −5 eV.

S–S bonds (i.e., σ^*_{P-S}, σ^*_{P-P}, or σ^*_{S-S}), which lie too high in energy to be good electron acceptors. As in the case of MPS_3 phases, therefore, the acceptor levels of the thiophosphates important for lithium intercalation are expected to be the empty or partially filled *d*-block levels of the transition metal rather than the σ antibonding levels of the ligands. Thus we carry out tight-binding band calculations (*21, 22*) on the transition metal thiophosphates, based upon the extended Hückel method, to examine the nature of their acceptor levels. To identify the molecular origin for those levels, we also perform MO calculations on molecular building blocks that represent the metal environments of the thiophosphates. Here we define each molecular building block of a thiophosphate as a molecular complex which contains two adjacent metal ions plus all their surrounding ligands. For convenience, we will discuss the octahedral and the bicapped trigonal bipyramid systems separately.

3.1. Octahedral Coordination

Each V^{3+} ion of $V_2P_4S_{13}$ is under an octahedral environment. Results of our tight-binding band calculations on $V_2P_4S_{13}$ and MO calculations on a bimetallic complex $(V^{3+})_2(P_4S_{13}^{6-})_4$, which represents the metal ion environment of $V_2P_4S_{13}$, are summarized in Fig. 2a. In Fig. 2, unless stated otherwise, the bands labeled by L have primarily ligand character while the rest of the bands have mainly metal ion *d*-orbital character. The bands indicated by * are degenerate, and the legend $m(d^n)$ means that a unit cell chosen for computation has *m* metal ions of configuration d^n. In Fig. 2a, the 12 *d*-block bands of $V_2P_4S_{13}$ originate from the t_{2g} levels of four V^{3+} ions. The t_{2g} levels of the molecular building block $(V^{3+})_2(P_4S_{13}^{6-})_4$ are shown on the right-hand side of Fig. 2a. The *d*-block bands of $V_2P_4S_{13}$ and the *d*-block levels of $(V^{3+})_2(P_4S_{13}^{6-})_4$ are closely spaced, since the $V^{3+} \cdots V^{3+}$ distance of 3.71 Å is too long for any direct metal–metal bonding. This is the reason $V_2P_4S_{13}$ exhibits paramagnetic properties (*9*).

3.2. Bicapped Trigonal Bipyramid Coordination

3.2.1. General feature. As will be seen later, the electronic structures of the *M*–P–S phases with bicapped trigonal bipyramid coordination are well described by those of the model clusters **29a–29c**. All the coordination sites of **29a** are occupied by S^{2-} ions except for the two S_2^{2-} ligands which form the rectangular face shared by the two bicapped prisms. This model **29a** is relevant in representing the metal ion environment of 2D-P_2NbS_8, 3D-P_2NbS_8, $TaPS_6$, and $Ta_4P_4S_{19}$. Shown in Fig. 3a are the first 10 *d*-block levels and the highest-lying ligand level calculated for the model cluster **29a**.[2]

[2] Model **29a** has the following interatomic distances: d_{M-M} = 2.86 Å, d_{S-S} = 2.02 Å (in S_2 pairs), d_{S-S} = 3.50 Å (between noncapping sulfurs), d_{S-S} = 3.22 Å (between capping and noncapping sulfur), and d_{M-S} = 2.62 Å (with capping sulfur). In **29b** and **29c**, the S_2^{2-} pairs at the extreme ends of the biprism are arranged such that the capping sulfur of each S_2^{2-} pair makes d_{M-S} = 2.55 Å and d_{S-S} = 3.22 Å.

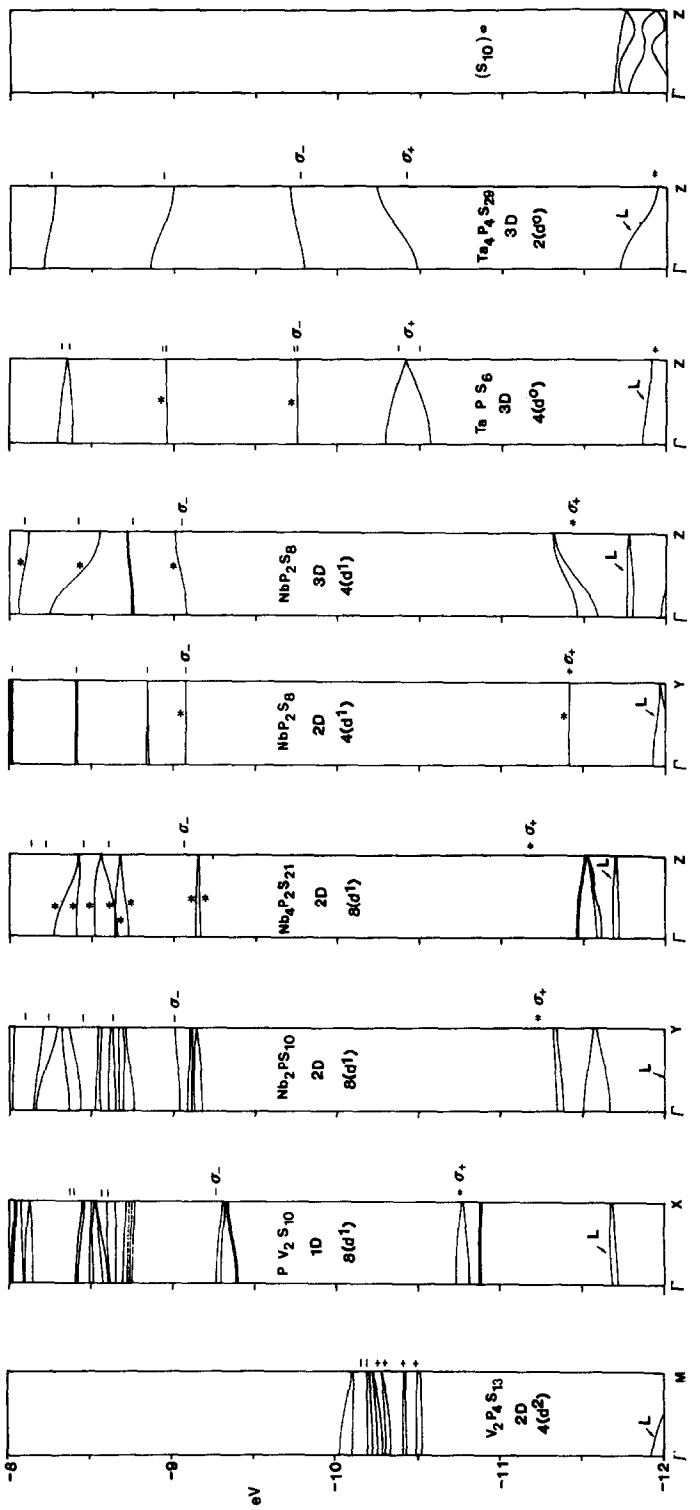

FIG. 2. Calculated energy bands of various thiophosphates that occur in the energy region between −12 and −8 eV, where $\Gamma = (0, 0, 0)$, $X = (a^*/2, 0, 0)$, $Y = (0, b^*/2, 0)$, $Z = (0, 0, c^*/2)$, and $M = (a^*/2, 0, -c^*/2)$ in the first Brillouin zone of the reciprocal space.

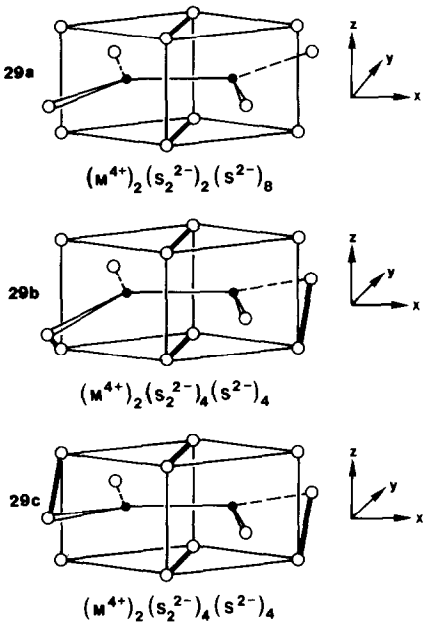

SCHEME 29

The orbital character for these *d*-block levels is shown in **30**, where, for simplicity, only the nodal properties of the metal *d*-orbitals are depicted. Though not shown, ligand orbitals of proper symmetry combine out of phase with the metal orbitals of **30**. Some of the high-lying orbitals of the two S_2^{2-} ligands are shown in **31** ($\phi_1 - \phi_7$). The ligand orbitals ϕ_1, ϕ_2, ϕ_3, ϕ_4, ϕ_5, and ϕ_6 combine out of phase with the *d*-block orbitals σ_-, π'_-, π_-, δ_-, σ_+, and π'_+, respectively. The ligand orbital ϕ_7 is found to combine out of phase with δ_+ and π_+.

The clusters **29b** and **29c** differ from cluster **29a** in that the former have two more S_2^{2-} ligands, each of which occupies both a capping and a prismatic coordination site. Clusters **29b** and **29c** have these two S_2^{2-} ligands arranged in such a way that they have the symmetry of twofold rotation and inversion, respectively. The cluster **29b** is relevant for PV_2S_{10} and $P_2Nb_4S_{21}$, and **29c** for PNb_2S_{10}. The *d*-block levels of the model clusters **29b** and **29c** are shown in Figs. 3b and 3c, respectively. It is observed that the *d*-block levels of **29b** or **29c** are very similar in nature to those of **29a** in that the σ_+ level is well separated from the rest of the metal *d*-block levels lying above. Due to the symmetry lowering on going from **29a** to **29b** or **29c**, the *d*-block levels of **29b** and **29c** lying above σ_- exhibit mixed orbital character of π_- and δ_- types. With d^1 metal ions such as V^{4+} or Nb^{4+}, the lowest-lying *d*-block level σ_+ is doubly filled, which is well separated from the LUMO σ_-.

In Fig. 3, the highest-lying ligand level (designated by L) has primarily the lone pair character of the S_2^{2-} ligands. The bimetallic centers such as **29a–29c** are the chromophores of the *M*–P–S phases. Based upon the highly symmetric model cluster **29a**, it can be easily shown that electronic

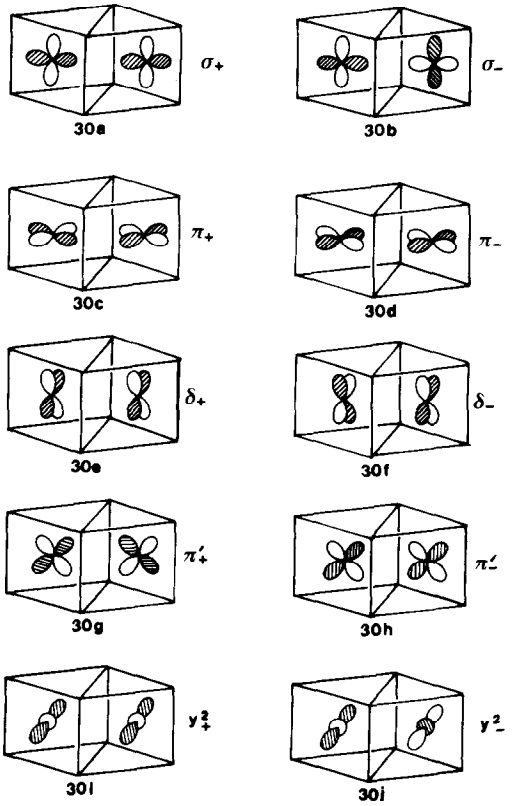

SCHEME 30

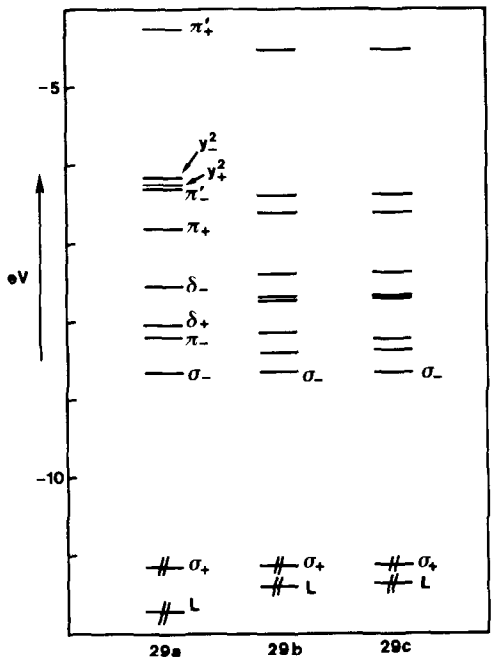

FIG. 3. Calculated MO energies for the model bimetallic cluster (a) **29a**, (b) **29b**, and (c) **29c**.

transition from the σ_+ level or the ligand level L is allowed to all the empty *d*-block levels lying above except to the δ_- and π'_- levels. In actual crystals of the *M*–P–S phases, their bimetallic centers have a lower symmetry than does **29a**. Thus, in those crystals, electronic transition from the σ_+ and the ligand levels L would be allowed to all the empty *d*-levels lying above. This would be responsible for the rich UV-visible spectra of PNb_2S_{10}, $P_2Nb_4S_{21}$, 2D-P_2NbS_8, and 3D-P_2NbS_8 with numerous absorption peaks (*26*).

3.2.1. PV_2S_{10}, PNb_2S_{10} and $P_2Nb_4S_{21}$. The band electronic structures of PV_2S_{10}, PNb_2S_{10}, and $P_2Nb_4S_{21}$ are shown in Figs. 2b, 2c, and 2d, respectively. The molecular building blocks for these compounds are bimetallic complexes $(M^{4+})_2(S_2^{2-})_4L_2$ (**32**), where M = V or Nb and $L = P_2S_8^{4-}$ or $P_2S_9^{4-}$. The short M^{4+}–M^{4+} distance (2.85 and 2.87 Å for M = V and Nb, respectively) indicates strong metal–metal bonding between adjacent metal ions. As indicated on the right-hand sides of Figs. 2b–2d, the two lowest-lying *d*-block levels of the molecular building blocks are primarily σ_+ and σ_- levels of the metal–metal bonds. As already noted from Fig. 3, the *d*-block bands arising from the σ_+ levels are well separated from those arising from the σ_- levels. Thus, with the formal oxidation of $M^{4+}(d^1)$, all the σ_+ bands in PV_2S_{10}, PNb_2S_{10}, or $P_2Nb_4S_{21}$ are fully occupied whereas all the σ_- bands are empty. Consequently, these thiophosphates are expected to be diamagnetic. This is the case for PNb_2S_{10} and $P_2Nb_4S_{21}$, but PV_2S_{10} is apparently paramagnetic. Thus it was suggested (*6*) that the short interligand S···S contacts in PV_2S_{10} (i.e., the S_{16}···S_{17} and S_{24}···S_{25} contacts in **32** are 2.972 and

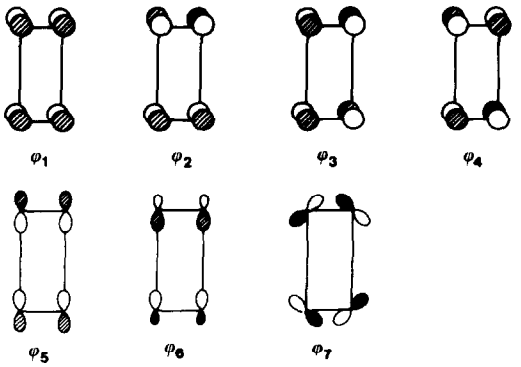

31

SCHEME 31

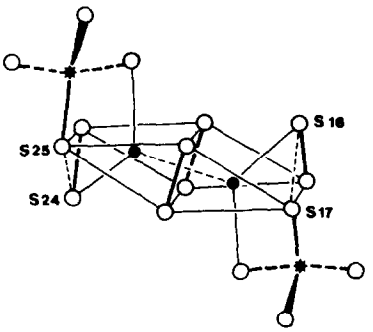

32

SCHEME 32

2.995 Å, respectively) have some covalent bonding character, thereby leaving slightly more than one *d*-electron per vanadium (i.e., d^{1+x} with $0 < x \ll 1$), which was thought to be responsible for the weak paramagnetic behavior. Similarly, trigonal prismatic complexes of dithiolate ligands, ML_3 (M = V, Re, Mo; L = $S_2C_2Ph_2$, $S_2C_2H_2$) (*27, 28*), have been found to have very short interligand S···S contacts. For instance the interligand S···S contacts of $V(S_2C_2Ph_2)_3$ are 2.927, 3.088, and 3.178 Å which led Eisenberg and co-workers to suggest the presence of bonding forces between such contacts. To test whether short interligand S···S contacts in PV_2S_{10} and $V(S_2C_2Ph_2)_3$ (*28*) have bonding interactions or not, we carry out MO calculations on the model complexes $(V^{4+})_2(S_2^{2-})_4(P_2S_8^{4-})_2$ and $V(S_2C_2H_2)_3$ (to simulate PV_2S_{10} and $V(S_2C_2Ph_2)_3$, respectively). Our MO calculations on $(V^{4+})_2(S_2^{2+})_4(P_2S_8^{4-})_2$ show that the overlap populations for the $S_{16}\cdots S_{17}$ and $S_{24}\cdots S_{25}$ contacts (see **32**) are all slightly negative (~ -0.03). Likewise, the overlap populations calculated in our work for the short interligands S···S contacts of $V(S_2C_2H_2)_3$ (i.e., the model for $V(S_2C_2Ph_2)_3$) are all slightly negative as well, regardless of whether we adopt the electron configuration leading to $V^{4+}[(S_2C_2H_2)_3]^{4-}$ or $V^{5+}[(S_2C_2H_2)_3]^{5-}$. That is, the S···S interactions in the short interligand S···S contacts are slightly antibonding. In addition, we observe that all the interligand S···S contacts in $(V^{4+})_2(S_2^{2-})_4(P_2S_8^{4-})_2$ and $V(S_2C_2H_2)_3$ have slightly negative overlap populations, and the shorter S···S contact leads to the more negative overlap populations. Therefore, the short S···S contacts cannot be considered to indicate the presence of covalent bonding interactions in those contacts. The short S···S contacts must occur largely because the V^{4+} (or V^{5+}) ion is small in size so that the ligands coordinating around each metal cation are squeezed to one another. According to this hypothesis, use of a larger metal cation would lead to longer interligand S···S contacts. **33a** shows the two shortest M···S and the shortest interligand S···S distances found for PV_2S_{10}, and **33b** those found for PNb_2S_{10}. As expected, the shortest S···S contact distance is longer in PNb_2S_{10} than in PV_2S_{10}, since Nb^{4+} ion is larger than V^{4+} ion so that the $Nb^{4+}\cdots S$ distances are longer than the corresponding $V^{4+}\cdots S$ distances. In other words, the short S···S contacts of PV_2S_{10} cannot be different from those of PNb_2S_{10} or $P_2Nb_4S_{21}$ in nature, and thus the paramagnetic properties of PV_2S_{10} must be due to impurity. This conclusion was recently confirmed. Magnetic susceptibility measurements on newly prepared PV_2S_{10} showed (*29*) that this compound is diamagnetic as predicted by the present study.

3.2.3. 2D- and 3D-P_2NbS_8. The molecular building blocks of 2D-P_2NbS_8 and 3D-P_2NbS_8 are given by $(Nb^{4+})_2(S_2^{2-})_2(P_2S_6^{2-})_4$ and $(Nb^{4+})_2(S_2^{2-})_2(PS_4^{3-})_4$, respectively. The band electronic structures of 2D-P_2NbS_8 and 3D-P_2NbS_8, and the *d*-block levels of their molecular building blocks, are shown in Figs. 2e and 2f, respectively. As in PV_2

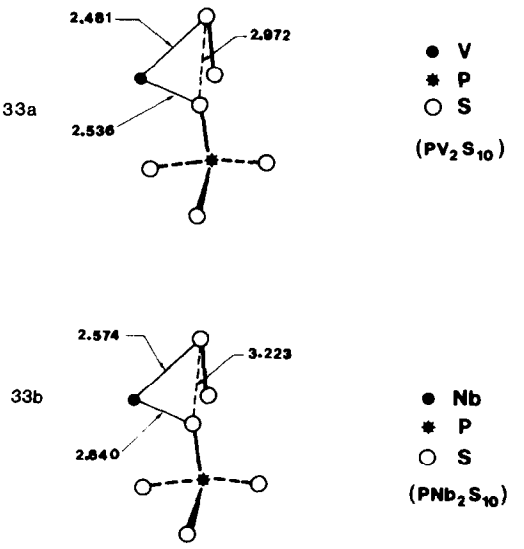

SCHEME 33

S_{10}, PNb_2S_{10}, and $P_2Nb_4S_{21}$, the empty *d*-block bands are all well separated from the fully filled σ_+ bands in 2D-P_2NbS_8 and 3D-P_2NbS_8.

3.2.4. $TaPS_6$ and $Ta_4P_4S_{29}$. The molecular building block representing the metal ion environment of $TaPS_6$ or $Ta_4P_4S_{29}$ is $(Ta^{5+})_2(S_2^{2-})_2(PS_4^{3-})_4$, see **20c** and **20d**. Because of the helix structures, $TaPS_6$ and $Ta_4P_4S_{29}$ (i.e., $[(TaPS_6)_8 + (S_{10})]/2$) are large for tight-binding band calculations. Thus we approximated the band electronic structures of $TaPS_6$ and $Ta_4P_4S_{29}$ by those of the model chains that are obtained when the molecular building blocks $(Ta^{5+})_2(S_2^{2-})_2(PS_4^{3-})_4$ are repeated along the *c*-axis (i.e., the axis of the helices). (For $Ta_4P_4S_{29}$, the $(S_{10})_\infty$ chain enclosed in each of the larger helix channels is taken into consideration later). The band electronic structures of these model chains for $TaPS_6$ and $Ta_4P_4S_{29}$ are shown in Figs. 2g and 2h, respectively, along with the *d*-block levels of their molecular building blocks, where all the *d*-block levels are empty. The energy separation between the σ_+ and σ_- levels is not as large as that in Figs. 2b–2f, since the $Ta^{5+}\cdots Ta^{5+}$ distance is long (3.383 Å). Shown in Fig. 2i is the band electronic structure of the $(S_{10})_\infty$ chain in the same energy region as that shown for the model chain in Fig. 2h. The bands of $(S_{10})_\infty$ are well separated from the *d*-block bands of Fig. 2h. The shortest S···S contacts between the $(S_{10})_\infty$ chain and its surrounding wall of the helix structure are ~3.3 Å. Such nonbonded S···S contacts do not involve any strong covalent interaction between the $(S_{10})_\infty$ chain and the wall of the helix structure. Thus superposition of the electronic structures of Figs. 2h and 2i would be a good approximation for the electronic structure of $Ta_4P_4S_{29}$.

4. Lithium Intercalation

When a host material has sites that can accommodate both electrons and Li^+ cations, lithium intercalation is facilitated. That is, for good lithium intercalation, a host should have a certain lattice structure (e.g., chain structure, layer structure, or three-dimensional structure with tunnels or interconnected cavities) that allows reversible insertion of Li^+ cations. In addition, the host should have low-lying acceptor levels (i.e., partially filled or empty orbitals) which can accommodate the electrons released by lithium. Well-known cathode materials for lithium batteries are layered transition metal dichalcogenides. For high-energy density batteries, it is necessary to have a host with numerous sites for both electrons and Li^+ cations. Thus transition metal compounds with high oxidation state of metal, provided that they also have enough Li^+ sites, are potential candidates for high-energy batteries since the partially filled or empty *d*-block orbitals of such compounds can in principle act as acceptor levels for electrons. Of course, it is conceivable that potential reduction sites other than metal cations (e.g., S_2^{2-} ligands) may be present in some compounds. Another important requirement for useful lithium batteries is that a host should maintain a high voltage discharge for a wide range of the lithium intercalation extent, *x*. Such a material will exhibit a relative flat voltage discharge curve at a high voltage level for a wide range of *x*.

All of the thiophosphates studied in our work have structural features favorable for accommodating Li^+ cations. For example, PV_2S_{10} has a chain structure. $V_2P_4S_{13}$, PNb_2S_{10}, $P_2Nb_4S_{21}$, and 2D-P_2NbS_8 have layer structures, and the three-dimensional compounds P_2NbS_8, $TaPS_6$, and $Ta_4P_4S_{29}$ have tunnels. Furthermore, the transition metal ions present in these thiophosphates are in relatively high oxidation states (e.g., V^{3+}, V^{4+}, Nb^{4+}, Ta^{5+}). It is quite clear from Fig. 2 that the acceptor levels important for lithium intercalation of the thiophosphates are their partially filled or empty *d*-block bands.

These bands are not very dispersive, and are very similar in energy to the *d*-block levels of their corresponding building units. This is so because the bimetallic centers of these thiophosphates are well separated from one another by phosphorus–sulfur polyanions.

As already mentioned, the σ^* levels of the S–S, P–S, and P–P simple bonds lie too high in energy to be good acceptor levels. Namely, phosphorus–sulfur polyanions and S_2^{2-} anions do not seem to be good reduction sites. Nevertheless, in a few well-studied materials such as Li_xTiS_3 (*30–32*) and Li_xFeS_2 (*33*) reduction of S_2^{2-} to $2S^{2-}$ has been observed to occur as lithium intercalation proceeds despite the fact that the σ^* levels of S_2^{2-} anions in TiS_3 lie well above the empty *d*-block levels: in $0 < x < 3$, Li_xTiS_3 consists of two separate phases, Li_3TiS_3 and TiS_3. In the former, there are no more S_2^{2-} ligands. In a recent study on Li_xTiS_3 (*34*), it was suggested that reduction of S_2^{2-} to $2S^{2-}$ is possible in TiS_3 if a *d*-block level of TiS_3 with the σ^* character of S_2^{2-} is occupied. This can occur when three electrons simultaneously enter each Ti^{4+} site of TiS_3. In the thiophosphates with bicapped trigonal bipyramid coordination as well, the σ^* orbital of S_2^{2-} (e.g., the orbital ϕ_7 in **31**) mixes into some *d*-block levels of their bimetallic centers (e.g., the δ_+ and π_+ levels of **29a**). In principle, therefore, electron occupation of such levels might lead to reduction of S_2^{2-} (however, our powder X-ray diffraction study on $Li_xPV_2S_{10}$ ($0 < x \leq 3$) prepared by chemical intercalation showed no significant change in diffraction patterns and in unit cell parameters). It seems therefore that lithium intercalation in PV_2S_{10} occurs without reducing S_2^{2-} into $2S^{2-}$, and $Li_xPV_2S_{10}$ remains a single phase during intercalation. In addition, our electrochemical intercalation study on $Li_xPV_2S_{10}$ ($0 < x \leq 8$) shows a relatively smooth voltage discharge curve with good reversibility, as shown in Fig. 4a. Consequently, it is reasonable to conclude that the reduction sites of PV_2S_{10} primarily responsible for lithium intercalation are the metal cations V^{4+} instead of the S_2^{2-} ligands or the S–S bonds of the phosphorus–sulfur polyanions. This conclusion should also be applicable for the other thiophosphates related to PV_2S_{10}.

Compared with the discharge curve of $Li_xPV_2S_{10}$ in Fig. 4a, $Li_xV_2P_4S_{13}$ system exhibits a relatively flat discharge curve at a high voltage, which is shown in Fig. 4b. Therefore, as a lithium battery material, V_2

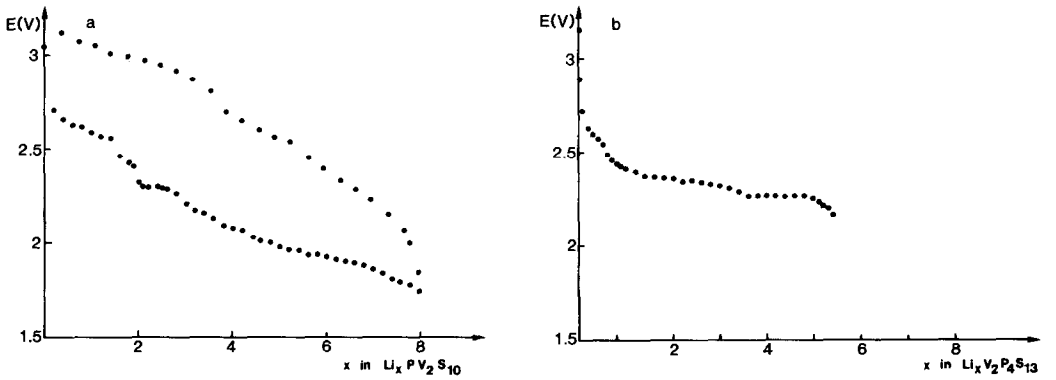

FIG. 4. Room temperature quasiequilibrium discharge curve of the (a) PV_2S_{10}/Li and (b) $V_2P_4S_{13}$/Li systems using 2 *M* $LiClO_4$ dissolved in dioxolane as electrolyte.

P_4S_{13} is expected to be better than PV_2S_{10} and its related systems. Comparison of Figs. 2a and 2b reveals that the presence of many acceptor levels in a narrow range of energy, as found for $V_2P_4S_{13}$, leads to a relatively flat discharge curve. As already discussed, the acceptor levels of $V_2P_4S_{13}$ are derived from the t_{2_g} orbitals of each V^{3+} center. Due to the long distance between the V^{3+} ions in each bimetallic center, the interaction between the two sets of t_{2_g} orbitals is weak so that the t_{2_g} block levels of $V_2P_4S_{13}$ occur in a narrow range of energy. For practical applications in lithium batteries, therefore, the $V_2P_4S_{13}$ phase appears more promising. Further studies on this and synthesis of its analogs are necessary.

5. Concluding Remarks

As discussed in detail in the previous sections, the *M*–P–S phases are best described as transition metal complexes with ligands S^{2-}, S_2^{2-}, and phosphorus–sulfur polyanions $P_nS_m^{x-}$. Band electronic structures calculated for the *M*–P–S phase and molecular electronic structures calculated for the molecular building blocks of the *M*–P–S phases clearly show that the low-lying acceptor levels of the *M*–P–S phases responsible for their lithium intercalation are the partially filled and/or empty *d*-block bands; i.e., the reduction sites of the *M*–P–S phases are their transition metal cations. This conclusion is in agreement with the results of our electrochemical lithium intercalation study on PV_2S_{10} and $V_2P_4S_{13}$. Our molecular orbital calculations also reveal that the extremely short interligand S···S contacts found for a few vanadium compounds exhibit negative overlap populations. Thus, such short S···S contacts are not caused by covalent bonding in those contacts, but should be regarded as a consequence of the small size of the vanadium cation, which squeezes its surrounding sulfur ligands close to one another.

Acknowledgment

This work was in part supported by the Camille and Henry Dreyfus Foundation through a Teacher–Scholar Award (1980–1985) to M.H.W., which made it possible for M.E. to visit the Department of Chemistry, North Carolina, State University and carry out the computations described herein.

References

1. G. Ouvrard, R. Brec, and J. Rouxel, *Mater. Res. Bull.* **20,** 1181 (1985).
2. R. Brec, G. Ouvrard, and J. Rouxel, *Mater. Res. Bull.* **20,** 1257 (1985).
3. E. Prouzet, G. Ouvrard, and R. Brec, *Mater. Res. Bull.* **21,** 195 (1986).
4. H. Hahn and W. Klingen, *Naturwissenschaften* **52,** 494 (1965).
5. W. Klingen, thesis, Höhenheim (1969).
6. R. Brec, G. Ouvrard, M. Evain, P. Grenouilleau, and J. Rouxel, *J. Solid State Chem.* **7,** 174 (1983).
7. G. Ouvrard, R. Brec, and J. Rouxel, *Ann. Chim. Fr.* **7,** 53 (1982).
8. R. Brec, R. Freour, G. Ouvrard, J. L. Soubeyroux, and J. Rouxel, *Mater. Res. Bull.* **18,** 689 (1983).
9. M. Evain, R. Brec, G. Ouvrard, and J. Rouxel, *J. Solid State Chem.* **56,** 12 (1985).
10. R. Brec, P. Grenouilleau, M. Evain, and J. Rouxel, *Rev. Chim. Miner.* **20,** 295 (1983).
11. R. Brec, M. Evain, P. Grenouilleau, and J. Rouxel, *Rev. Chim. Miner.* **20,** 283 (1983).
12. P. Grenouilleau, R. Brec, M. Evain, and J. Rouxel, *Rev. Chim. Miner.* **20,** 628 (1983).
13. M. Evain, R. Brec, G. Ouvrard, and J. Rouxel, *Mater. Res. Bull.* **18,** 41 (1984).
14. S. Fiechter, W. F. Kuhs, and R. Nitsche, *Acta Crystallogr. B* **36,** 2217 (1980).
15. M. Evain, M. Queignec, R. Brec, and J. Rouxel, *J. Solid State Chem.* **56,** 148 (1985).
16. A. H. Thompson and M. S. Whittingham, U.S. Patent 4,049,879 (1977).
17. R. Brec and A. Lemehaute, Fr. Patents 7,704,518 and 7,704,519 (1977).
18. M.-H. Whangbo, R. Brec, G. Ouvrard, and J. Rouxel, *Inorg. Chem.* **24,** 2459 (1985).
19. H. Mercier, Y. Mathey, and E. Canadell, *Inorg. Chem.* **26,** 963 (1987).
20. R. Hoffmann, *J. Chem. Phys.* **39,** 1397 (1963).
21. M.-H. Whangbo and R. Hoffmann, *J. Amer. Chem. Soc.* **100,** 6093 (1978).
22. M.-H. Whangbo, R. Hoffmann, and R. B. Woodward, *Proc. R. Soc. London Ser. A* **366,** 23 (1979).

23. G. OUVRARD, R. FREOUR, R. BREC, AND J. ROUXEL, *Mater. Res. Bull.* **20,** 1053 (1985).
24. V. W. KRÖNERT AND F. PLIETH, *Z. Anorg. Allg. Chem.* **336,** 207 (1965).
25. S. FURUSETH, L. BRATTÅS, AND A. KJEKSHUS, *Acta Chem. Scand. A* **29,** 623 (1975).
26. M. QUEIGNEC, M. EVAIN, R. BREC, AND C. SOURISSEAU, *J. Solid State Chem.* **63,** 89 (1986).
27. E. I. STIEFEL, R. EISENBERG, R. C. ROSENBERG, AND H. B. GRAY, *J. Amer. Chem. Soc.* **88,** 2956 (1966).
28. R. EISENBERG AND H. B. GRAY, *Inorg. Chem.* **6,** 1844 (1967).
29. M. EVAIN, thesis, Nantes (1986).
30. R. R. CHIANELLI AND M. B. DINES, *Inorg. Chem.* **14,** 2417 (1975).
31. S. P. GWET, thesis, Paris (1983).
32. P. GARD, thesis, Bordeaux (1986).
33. P. GARD, C. SOURISSEAU, G. OUVRARD, AND R. BREC, *Solid State Ionics* **20,** 231 (1986).
34. E. CANADELL (private communication).
35. H. BASCH, A. VISTE, AND H. B. GREY, *Theor. Chim. Acta* **3,** 458 (1965).
36. J. H. AMMETER, H. B. BÜRGI, J. C. THIBEAULT, AND R. HOFFMANN, *J. Amer. Chem. Soc.* **100,** 3686 (1978).